

Research on Resistance Characteristics of Fire Zone of Mine Tunnel Fire and Construction of Calculation Model

Minghao Ni ^{1,*}, Xiaokun Zhao ^{1,*}, Wencai Wang ², Qiongyue Zhang ³, Hongwei Wang ¹ and Jianing Wang ¹

¹ School of Coal Engineering, Shanxi Datong University, Datong 037009, China

² School of Mining and Coal, Inner Mongolia University of Science and Technology, Baotou 014010, China

³ School of Mechanical and Materials Engineering, North China University of Technology, Beijing 100144, China; zqynm1998@163.com

* Correspondence: 220857002156@sxdtdx.edu.cn (M.N.); 19835125355@163.com (X.Z.)

Abstract: To investigate resistance change in the fire area of a roadway caused by roadway fires, a mathematical calculation model for thermal resistance is developed. Theoretical research is conducted to analyze the factors influencing resistance change through theoretical derivation, revealing that temperature is a key factor contributing to the change in thermal resistance. By leveraging the correlation between changes in CO concentration and temperature on the downwind side of the roadway within the fire zone, researchers developed mathematical models to predict temperature increases at various points downwind of the fire source. These models were then used to determine the mathematical relationship governing the change in thermal resistance. The accuracy of the numerical simulation software was validated using Fluent numerical simulation software and scaled-down model experiments. Full-scale numerical simulation experiments were conducted to investigate the fire characteristics of roadway fires and validate the thermal resistance mathematical model. The results indicate that the thermal resistance in the numerical simulation is 7.55 Pa at 20m from the fire source and 5.54 Pa at the end of the roadway. The decrease in resistance is linear. The minimum error between the thermal resistance calculated by the mathematical model and the gradient of the pressure drop in the numerical simulation is 0.03 Pa, approximately 2.3%. Furthermore, the fitting degree of the pressure drop in each section is as high as 97.7%. The calculation model demonstrates high accuracy and offers a theoretical foundation for investigating fire resistance in tunnel fire.

Keywords: thermal resistance; theoretical derivation; mathematical modelling; scaled model experiments; numerical simulation



Citation: Ni, M.; Zhao, X.; Wang, W.; Zhang, Q.; Wang, H.; Wang, J. Research on Resistance Characteristics of Fire Zone of Mine Tunnel Fire and Construction of Calculation Model. *Fire* **2024**, *7*, 197. <https://doi.org/10.3390/fire7060197>

Academic Editors: Yanming Ding, Kazui Fukumoto and Jiaqing Zhang

Received: 1 June 2024
Revised: 12 June 2024
Accepted: 12 June 2024
Published: 13 June 2024



Copyright: © 2024 by the authors. Licensee MDPI, Basel, Switzerland. This article is an open access article distributed under the terms and conditions of the Creative Commons Attribution (CC BY) license (<https://creativecommons.org/licenses/by/4.0/>).

1. Introductory

Mine fires are a significant concern among scholars worldwide, with 60% of coal mine fires being exogenous fires. Among these, tape fires are the most prevalent, often caused by prolonged friction between the tape and bottom rollers during the conveying process. This friction can lead to temperature increases, igniting any coal residue present. When a fire breaks out in a mine, it typically alters the ventilation resistance of the affected area, impacting the ventilation system and creating turbulence in the underground airflow [1] (pp. 273–276). Once ignited, toxic gases like carbon monoxide (CO) emitted by the fire can quickly escalate and spread to unaffected areas, posing a threat to the safety of individuals and the overall evacuation process. Scholars both domestically and internationally have extensively researched the evolving characteristics of fire zone resistance. These studies have focused on the contributing factors to fire zone resistance resulting from fires as well as the impact of variables such as fire source intensity, ventilation conditions, elevation of the fire zone tunnel, and other related factors on the magnitude of resistance. Zhou Chuang [2] (pp. 24–26) and colleagues conducted scaled-down model experiments and numerical simulations to study mine ventilation resistance in the presence of a uniform heat source. By integrating theoretical principles of thermodynamics and the equation of energy

conservation, they developed a model for calculating the thermal resistance of a tunnel with a uniform heat source; Li Zongxiang [3] (pp. 909–913) and other researchers conducted a study on local resistance and resistance coefficient of flames using mathematical derivation methods. They explained the relationship between the size of the cross-sectional area of the fire source and local resistance, provided formulas for local resistance and resistance coefficient, and validated their mathematical models through experiments. In the study of flame shape and cross-section, Ward-Smith [4] has investigated the one-dimensional flow of smoke generated by fires by means of a one-dimensional treatment of alley fires and has constructed and optimized the differential equations for the viscous losses in the combustion zone of their flow processes by means of theoretical derivations. Fu Peifang et al. [5–7] examined the thermal dynamics of fires on roadways, demonstrating the physical significance of thermal dynamics through numerical simulations and scaled-down model experiments. They also determined the relationship between the pressure change gradient due to thermal resistance and the distance from the fire source.

Numerous scholars have discovered that thermal resistance arises from the heating of air by a fire source, causing changes in its density and other factors that impact its resistance [8,9]. In the study, a strong correlation was observed between the thermal resistance magnitude and the degree of temperature rise. George and Davood [10] used numerical simulation to study the heat transfer of the wind flow in a roadway fire, which mainly used Multiflux and CFD numerical simulation software to illustrate the laws of heat and mass transfer of the wind flow. OKA Y et al. [11–13] conducted scaled-down model experiments to examine the longitudinal position and temperature variation of the smoke layer in a fire tunnel. They predicted temperature and wind speed variations and proposed a mathematical model for analysis; Kalech et al. [14] (pp. 1034–1040) conducted a study on the high temperature smoke from tunnel fires in ventilated environments. They utilized FDS numerical simulation software to illustrate the temperature distribution and CO distribution characteristics. In studies conducted by various scholars on local fire zone resistance, a key consideration is the presence of a uniform heat source. However, in real mine fires, the temperature downstream of the fire source varies with distance and is not evenly distributed. Additionally, after a fire, the temperature of the tunnel in its fire zone is strongly related to the ventilation conditions [15,16]. The study aims to analyze the temperature change within a tunnel in a fire zone and incorporate it into the calculation of thermal resistance. This approach can enhance the accuracy of calculating the fire zone resistance. Additionally, the research investigates the components of fire zone resistance and develops a calculation model for fire zone resistance. This model can offer theoretical support for determining ventilation resistance and restructuring the wind network during fire incidents.

2. Theoretical Study on the Change of Tunnel Wind Resistance during the Catastrophic Period

When a fire occurs in a tunnel, the total resistance in the tunnel can be broken down into the ventilation resistance on the upwind side of the fire source, the local resistance of the fire source, and the thermal resistance on the downwind side of the fire source, as illustrated in Figure 1.

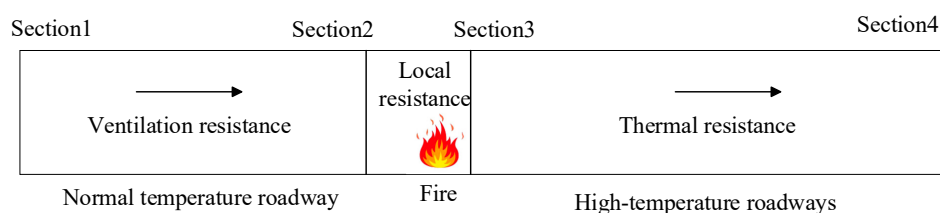


Figure 1. Composition of roadway resistance.

Division of the tunnel into 4 intervals, with the numbers at the top of the model representing the interval segments. When the wind speed in the horizontal roadway exceeds the critical wind speed, the high-temperature smoke generated by the fire source has minimal impact on the upwind side, with only local resistance present. In this scenario, the ventilation resistance for Sections 1–2 on the upwind side of the fire source can be calculated using Equation (1), which represents the formula for ventilation resistance.

$$h_{1-2} = (p_1 - p_2) + \left(\frac{\rho_1 v_1^2}{2} - \frac{\rho_2 v_2^2}{2} \right) \tag{1}$$

The ventilation resistance from Section 1 to Section 2 is represented by h_{1-2} , measured in Pa. The full pressure of Sections 1 and 2 is denoted by p_1 and p_2 , respectively, in Pa. The density of the fluid in Sections 1 and 2 is indicated by ρ_1 and ρ_2 , measured in Kg/m^3 . The fluid flow rate at Sections 1 and 2 is represented by v_1 and v_2 , m/s. In Figure 1, Sections 2–3 discuss the local resistance, which is primarily attributed to the wind flow passing by the fire source. The fire plume creates a wind barrier that hinders the passing wind flow, resulting in an additional loss of local resistance to the thermal bypass flow. Equation (2) shows the expression for the local resistance $h'_{e,r}$.

$$h'_{e,r} = \frac{1}{2} \zeta \rho' v'^2 \tag{2}$$

where λ is the flame local resistance coefficient, ρ' is the density of the wind flow through the exit of the fire zone in kg/m^3 , and v' is the exit wind speed in m/s.

The expression for the local resistance coefficient is related to the size of the flame section in accordance with the empirical formula for roadway ventilation. By considering the local resistance, we can obtain the following expressions for local resistance and the local resistance coefficient.

The relationship between the local resistance of the flame and the cross-sectional area of the flame can be observed in Equations (3) and (4).

$$h'_{e,r} = \frac{1}{2} \rho' v'^2 \left(\frac{1.7S_y}{S - S_y} \right)^2 \quad (S_y < S) \tag{3}$$

$$\zeta = \left(\frac{1.7S_y}{S - S_y} \right)^2 \quad (S_y < S) \tag{4}$$

When the horizontal dimensions of the fire source remain constant or change minimally, there is a correlation between the flame height and the rate of heat release [17,18], which can be characterized by Equation (5).

$$\frac{L}{D} = -1.02 + 3.7Q^{*\frac{2}{5}} \tag{5}$$

where L is the flame height, m; D is the equivalent diameter of the fire source, m; and Q^* is the dimensionless heat release rate, which is calculated as Equation (6).

$$Q^* = \frac{Q}{\rho C_p T_0 g^{1/2} H^{5/2}} \tag{6}$$

The flame height can be calculated using Equations (5) and (6), and then multiplied by the horizontal size of the fire source to determine the fire stage area. This helps in assessing the resistance to bypassing flow due to the fire source. In these equations, Q represents the heat release rate in Kw, c_p is the specific heat capacity of ambient air at constant pressure in $\text{Kj}/(\text{kg}\cdot\text{K})$, T_0 is the ambient temperature in K, g is the acceleration of gravity in m/s^2 , and H is the hydrodynamic diameter in m.

3. Research on the Construction of Thermal Resistance Model of Fire Zone Roadway

Figure 2 depicts an experiment on one-dimensional inviscid pipeline thermal resistance. The high-quality interface pipeline connects to an infinite container, assuming no heat or work exchange with the environment and no viscosity within the pipeline. This setup enables the derivation of conservation equations, as shown in the experimental schematic diagram below.

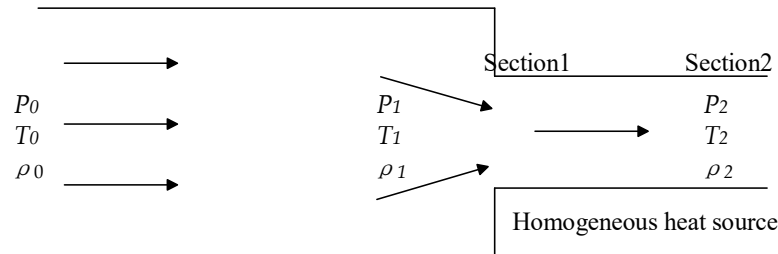


Figure 2. Schematic diagram of experimental thermal resistance of non-adhesive pipe.

In Figure 2, P_0 is the pressure of the ambient ventilation, pa; T_0 is the temperature of the ambient airflow, K; ρ_0 is the density of the ambient airflow, Kg/m³; P_1 is the pressure of the airflow into the inlet of the heated tunnel, pa; T_1 is the temperature of the airflow at the inlet of the heated tunnel, K; ρ_1 is the density of the airflow at the inlet of the heated tunnel, Kg/m³; P_2 is the pressure of the airflow at the outlet of the heated tunnel, pa; T_2 is the temperature of the airflow at the exit of the heated tunnel, K; and ρ_2 is the density of the airflow at the exit of the heated tunnel, Kg/m³; Section 1 and Section 2 representing the entrance and exit sections of a heated tunnel.

The continuity equation for its tube flow experiment can be expressed by Equation (7):

$$\rho_1 v_1 = \rho_2 v_2 \tag{7}$$

The momentum equation can be expressed by Equation (8):

$$p_1 + \rho_1 v_1^2 = p_2 + \rho_2 v_2^2 \tag{8}$$

In the experimental setup, P_1 and P_2 represent the pressures in Sections 1 and 2 respectively, Pa; while ρ_1 and ρ_2 denote the densities of the fluid in Sections 1 and 2, measured in kilograms per cubic meter, Kg/m³. Similarly, v_1 and v_2 represent the flow rates in Sections 1 and 2, measured in m/s. By combining Equations (7) and (8), we derive Equation (9).

$$p_1 - p_2 = \rho_1 v_1 (v_2 - v_1) \tag{9}$$

When fluid enters a heated pipe, the physical properties of the fluid cause accelerated thermal expansion, resulting in $v_2 - v_1 > 0$, or $p_1 - p_2 > 0$. This indicates that the pressure at Section 1 is greater than the pressure at the exit of Section 2. This phenomenon and its calculations can be described as a pressure drop in the direction of fluid flow due to heat in the pipeline, which can be referred to as thermal resistance.

Thermal resistance causes pressure changes at both ends of the fluid, leading to the construction of a thermal resistance coefficient based on the frictional resistance factor, as described in Equation (10).

$$C_t = \frac{(p_1 - p_2)}{(\rho_2 v_2^2 / 2)} \tag{10}$$

The energy equation is Equation (11):

$$c_p T_1 + \frac{v_1^2}{2} + e + gz_1 = c_p T_2 + \frac{v_2^2}{2} + gz_2 \tag{11}$$

where c_p is the specific heat capacity of the fluid at constant pressure, in J/(kg × K); T_1 and T_2 represent the temperatures of Sections 1 and 2 of the wind flow in K; e is the heat absorption per 1 kg of wind flow passing from Section 1 to Section 2, calculated as $e = Q/q_m$, in J/kg; Q is the heat transferred to the wind flow from Section 1 to Section 2 per unit time, J; and q_m is the mass flow rate of the fluid, kg/s.

Scholar Yang Shengqiang [17] (pp. 630) proposed using the equivalent unheated viscous flow control equation with the equivalence condition to derive a factorless criterion for obtaining the formula for thermal resistance, see Equation (12).

$$h_t = C_t \rho_2 v_2^2 / 2 \quad (12)$$

where the thermal resistance coefficient C_t is expressed in Equation (13) after the introduction of the factorless criterion:

$$C_t = \frac{2H_e}{1 + H_e + H_{e1}} \quad (13)$$

The factorless criterion, denoted as H_e , is defined as $H_e = e/c_p T_0$, where e represents the heat applied and $c_p T_0$ is the initial enthalpy of stagnation for a unit mass of fluid flowing from Cross Section 1 to Cross Section 2. Additionally, H_{e1} is defined as $g(z_1 - z_2)/c_p T_0$, where g is the gravitational acceleration, z_1 and z_2 are the heights of Cross Section 1 and Cross Section 2 respectively, and $c_p T_0$ is the initial enthalpy of stagnation.

The thermal resistance coefficient C_t in Equation (13) can be determined based on its relationship with temperature. The formula for temperature distribution in Figure 2 serves as a standard, where fluid enters the heated area due to a uniform heat source. In actual mine fires, factors such as wind flow velocity, heat release rate of the fire source, distance from the source of the fire, and other variables impact the temperature of the area. Changes in temperature lead to variations in thermal resistance, with local temperature depending on distance from the fire source. Applying the relevant rules to the calculation of the thermal resistance coefficient can enable the newly constructed model to more accurately reflect the size of the thermal resistance.

4. Study on the Characteristics of Temperature Change in the Roadway in the Fire Zone

4.1. Characterisation of the Difference between CO Concentration and Temperature Variation on the Downwind Side of a Fire Source

Changes in CO concentration are primarily attributed to the presence of the flue gas layer above and the air below, creating a “dilution” effect on the control. Additionally, temperature decay occurs as a result of heat transfer from the high temperature flue gas to the surrounding wall as well as the cooling effect of the suction of cold air, leading to a decrease in temperature. As wind speed increases, the wind flow shear effect enhances the attenuation effects of CO concentration and temperature. This leads to differences in the attenuation of CO concentration and temperature due to various control mechanisms. However, both are influenced by the spreading of the carrier flue gas layer and the wind flow, resulting in a certain degree of consistency and universality in the attenuation patterns studied.

Hu Longhua [18–21] developed a mathematical model to analyze the change in temperature rise based on variations in CO concentration. This was achieved through numerical simulations, full-scale experiments, and mathematical derivations to distinguish the CO concentration within the fire zone of the roadway. Additionally, a dimensionless approach was applied to the CO content and temperature rise. The CO concentration decay pattern has an inverse decay, which can be described as Equation (14):

$$\frac{C_x}{C_0} = \frac{1}{1 + bx} \quad (14)$$

where C_x represents the CO content at a distance of x_m from the location of the fire source, mol/mol; C_0 is the increase in CO content directly above the fire source in the environment,

mol/mol; x is the distance from the fire source in m; and b is the attenuation factor, which can be expressed as shown in Equation (15).

$$b = \frac{\rho_a \beta W |u - u_s|}{m_0} \tag{15}$$

where ρ_a represents the density of air in kg/m^3 ; W stands for the width of the lane in m; u is the inlet fluid velocity in meters per second; u_s is the fluid velocity at the x -point in meters per second; and m_0 denotes the flow rate of the flue gas directly above the fire source in kg/s ; β is a dimensionless parameter that can be calculated using Equation (16);

$$\beta = -\frac{d\bar{p}/dy}{\bar{p}} \tag{16}$$

The difference result can be obtained after the dimensionless processing of CO concentration change and temperature change. The results are given in Equation (17)

$$\frac{C_x}{C_0} - \frac{\Delta T_x}{\Delta T_0} = \lambda(1 - e^{-Kx}) \tag{17}$$

ΔT_x represents the dimensionless temperature rise at x_m from the fire source, while ΔT_0 indicates the dimensionless temperature rise directly above the fire source. λ is the dimensionless constant and K is the temperature attenuation coefficient, also dimensionless.

Where λ can be expressed as Equation (18)

$$\lambda = \frac{1}{1 + \frac{\rho_a \beta |u - u_s| L}{m_0}} \tag{18}$$

where L denotes the characteristic length, m. Its physical meaning is the distance to infinity at which the thermal buoyancy effect of the smoke layer decays and is expressed as $L = \frac{c_p m_0}{hP}$, where h denotes the thickness of the smoke layer, m; P denotes the atmospheric pressure, pa. Some scholars verified its coefficients under the working condition of normal air pressure and obtained its constant expression about the change of wind speed, see Equation (19).

$$\lambda = \frac{1}{3.26 + 0.931u} \text{ (1atm)} \tag{19}$$

Its temperature attenuation coefficient, K , can be described by Equation (20).

$$K = \frac{\alpha D}{c_p \dot{m}} \tag{20}$$

In the formula, D represents the length of the smoke layer in contact with the roadway wall in m, while α indicates the heat transfer coefficient in $\text{W}/(\text{m}^2 \cdot \text{K})$ when the smoke layer is not in contact with the ground. The convective heat transfer coefficient is denoted as h_c in $\text{W}/(\text{m}^2 \cdot \text{K})$, and the radiative heat transfer coefficient is represented as h_r in $\text{W}/(\text{m}^2 \cdot \text{K})$. When the smoke layer is in contact with the ground, the calculation formula is applied as: $\alpha = h_c + h_r$.

4.2. Multi-Unit Regional Thermal Resistance Modelling

By performing the relevant conversions of Equations (12) and (13), if there is no height difference in the roadway, the thermal resistance equation can be obtained using Equation (21):

$$h_t = \frac{e \rho_2 v_2^2}{c_p T_0 + e} \tag{21}$$

The ρ_2 and v_2 represent the air density and wind speed on the downwind side of a uniform heat source, respectively. However, in a real fire scenario, the density and wind speed may vary across different areas on the downwind side. To address this, it is suggested to divide the downwind side of the roadway near the fire source into multiple unit areas. By applying the ideal gas equation, the wind speed and density of the downwind side of the fire can be calculated and expression of the Equations (22) and (23)

$$v_h = v_T \frac{T_h}{T_T} \tag{22}$$

$$\rho_h = \rho_T \frac{T_T}{T_h} \tag{23}$$

where the corner scale T represents the ambient temperature, K, and the corner scale h represents the temperature on the downwind side, K. The downwind side of the fire source is divided into several unit regions, which are shown schematically in Figure 3.

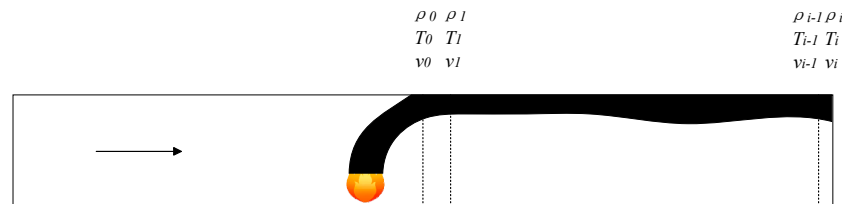


Figure 3. Schematic diagram of unit area division.

In Figure 3, 0 is the initial interval segment, and the downwind side of the fire source is divided into i intervals, where ρ represents the density, Kg/m^3 ; T represents the wind flow temperature, K; and v represents the flow velocity, m/s , and its corner markers represent the interval segments in which they are located, e.g., ρ_0 is the density of the 0th interval segment after the fire source, Kg/m^3 T_0 is the wind flow temperature of the 0th interval segment after the fire source, K; and v_0 is the flow velocity of the wind flow of the 0th interval segment after the fire source, m/s .

The expression for the wind speed in the i th interval segment by replacing the corner scale T in Equations (22) and (23) with the temperature in the previous interval segment is Equation (24)

$$v_i = v_{i-1} \frac{T_{i-1}}{T_i} \quad (i \geq 1) \tag{24}$$

Their density meter and Equation (24) calculation method are known; Equation (21) can be obtained on the multi-unit region of the thermal resistance calculation model, which is modelled as Equation (25).

$$h_t = \sum_{i=1}^L \frac{e\rho_{i-1}v_{i-1}^2}{c_p T_{i-1} + e} \cdot \frac{T_i}{T_{i-1}} \tag{25}$$

The transformation of Equation (17) leads to Equation (26).

$$\frac{\Delta T_x}{\Delta T_0} = \frac{\frac{C_x}{C_0} - \lambda}{1 - \lambda} \tag{26}$$

Combined with Equations (14), (15), and (19), Equation (26) can be converted to obtain the relationship between temperature decay with distance and wind speed. The formula is shown in Equation (27).

$$\frac{\Delta T_x}{\Delta T_0} = \left(\frac{3.26 - 0.931v}{2.26 - 0.931v} \right) \left(\frac{m_0}{m_0 + \rho_a W v x} \right) - \frac{1}{2.26 - 0.931v} \tag{27}$$

Substituting Equation (27) into Equation (25) yields the final model for calculating the thermal resistance of the multi-unit area.

Combining the local resistance and ventilation resistance in the fire zone, the fire zone roadway resistance model can be obtained, which is modelled as Equation (28).

$$\begin{aligned} H_t &= h_r + h_t + h'_{e,r} \\ &= h_r + \frac{1.7s_y \rho v^2}{2(s - s_y)} + \sum_{i=1}^L \frac{e \rho_{i-1} v_{i-1}^2}{c_p T_{i-1} + e} \cdot \frac{T_i}{T_{i-1}} \end{aligned} \quad (28)$$

5. Experimental and Numerical Simulation of a Reduced Scale Model

5.1. Experimental Platform Construction

During a visit to a mining enterprise in Shanxi Province, a scaled-down model of a roadway section measuring 4 m × 5 m was established. The model was created based on the principles of power similarity and motion similarity in hydrodynamics, ensuring that it was isometrically scaled with the actual model [22–24] (pp. 179). The scaling relationship can be described by the formula:

$$\lambda_l = \frac{l_m}{l_p}$$

where λ is the scaling relationship between the scaled model and the full-size model, l is the feature length, m is the scaled model corner scale, and p is the full-size model corner scale.

A scaled model with a geometrically similar scale relationship of approximately 6.5 is employed for fire experiments. The model's layout is divided into 10 sections to optimize sensor placement. To ensure the precision of experimental results, an adiabatic coating is applied to the model's roof to prevent heat loss and external heat exchange. Detailed parameters for each section of the model can be found in Table 1.

Table 1. Tunnel modelling parameters.

Place	Size (cm)	Material
Awning	80 × 100	stainless steels
Bottoms	80 × 100	stainless steels
Frame	3.8 × 3.8	square aluminum tubes
Wall	60 × 100	reinforced glass
Fire	20 × 30 × 1.5	aluminum
Bottom height above ground	40	-

The model is shown in Figure 4.



Figure 4. Model drawing of tunnel scaling.

Temperature sensors and gas concentration sensors are positioned at the top of the model, with wind speed sensors placed at the exits, entrances, and connections within the model. Additional sensors are located in the middle of the model's roof. The temperature sensor utilizes a Pt-100 thermocouple, while the gas concentration sensor is part of a multi-gas detection device capable of detecting O₂, CO, and CO₂ concentrations.

At an ambient temperature of 25 °C, several pt100-type thermocouples and gas concentration sensors were strategically placed on the top of the scale model to monitor temperature and CO₂ concentration variations in real-time during a fire event. The fire source was positioned 300 cm away from the model entrance, with the first sensor directly above it. Subsequent sensors were placed at 50 cm intervals in the downwind direction, and a final set of sensors were positioned at the end section of the model.

All sensors transmit real-time detection data to a computer via an RS485 communication line for recording purposes. The model layout is depicted in Figure 5.

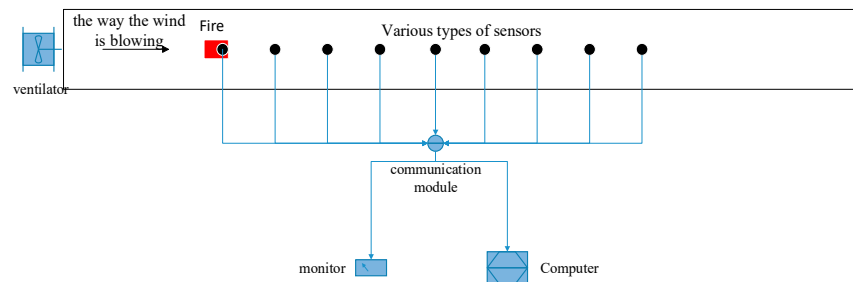


Figure 5. Drawing of the structure of the scaled-down model.

In Figure 5, the red color represents the location of the fire source, the blue color represents the detection and fan equipment, the arrow shows the direction of the wind flow, the black dots are the sensor deployment locations, and the blue line segments are the communication lines between the monitoring equipment.

The ignition source material, ethanol, with the chemical formula C₂H₆O, was chosen, and its material properties are shown in Table 2.

Table 2. Incendiary properties.

Characteristic	Parameters
density/(kg/m ³)	800
flash point/°C	12
combustion heat/(KJ/kg)	29,710
boiling/°C	78.4
latent heat of evaporation/(KJ/kg)	845.2
concentration/%	>99

The ambient temperature was determined to be 25 °C and the fire experiment was conducted using its model, which was first analyzed for its O₂ and CO₂ variations, which are plotted in Figure 6.

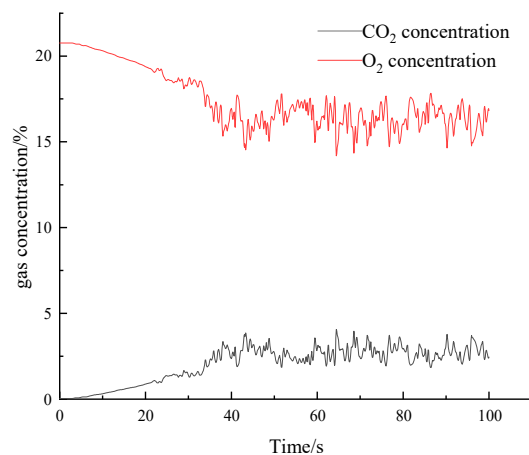


Figure 6. Plots of O₂ and CO₂ concentration changes.

The graph illustrates that the O₂ concentration initially drops to its lowest point around 40 s, whereas the CO₂ concentration peaks for the first time. Subsequently, both gas concentrations fluctuate within a narrower range but remain relatively stable. This pattern of fluctuation is observed for both gases. Therefore, it can be proved that in about 40 s, its combustion state reaches the fire stability stage. The numerical simulation software Fluent2023 R2 was used to simulate the scaled fire model, and its boundary conditions and the scaled model for the same settings were used to obtain the temperature distribution of each measurement point at 40 s, as shown in Figure 7.

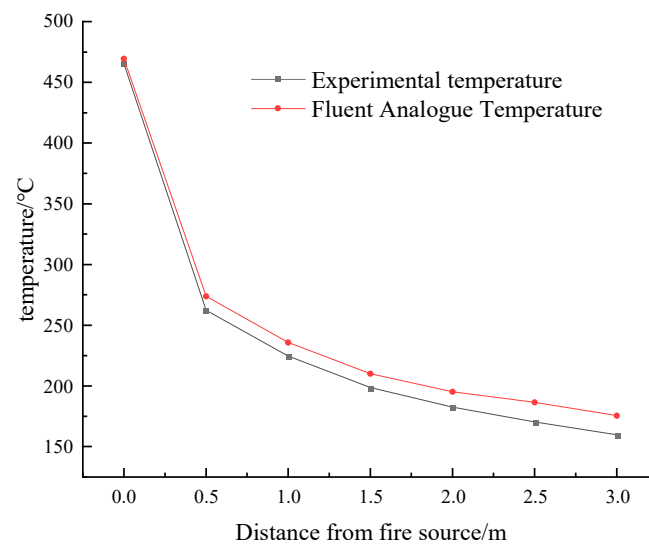


Figure 7. Plot of 40 s numerical simulation versus experimental temperature.

In the stable phase of the fire, the temperature decay of the two experiments aligns with exponential decay as the distance from the fire source increases, as illustrated in Figure 7. The temperature in Fluent appears relatively higher compared to the experiments, primarily due to the ideal conditions in Fluent. In the scaled model experiments, despite the use of thermal insulation coatings on the wall, heat exchange with the environment still occurs, leading to heat loss. Consequently, the numerical simulation shows slightly higher temperatures compared to the scale model experiment. The consistency in temperature trends suggests that the simulation of fire on the roadway using numerical simulation software Fluent2023 is highly reliable.

By analyzing the numerical simulated values and the temperature values of the scaled model experiments, the methodology for error calculation can be described using the equation found in the literature [25]. It is mathematically modelled as Equation (29):

$$\delta = (\Delta/L) \times 100\% \quad (29)$$

where δ is relative error, Δ is absolute error, and L is real value. For this section, the value is taken for the numerical solution. The error is calculated to be about 2.9%. Thus, its simulation accuracy is high.

5.2. Numerical Simulation Models

In fire simulation, the main numerical simulation software includes Fluent2023 and FDS. The choice of turbulence model and combustion model is crucial in fire simulation. Fluent offers a variety of turbulence model options, while FDS primarily focuses on the LES turbulence model. Research by Maele [26] has shown that the LES turbulence model yields a higher critical wind speed compared to other turbulence models. Ventilation conditions in mines have a significant impact on roadway fires. McGrattan [27] emphasizes that when considering different CFD models for specific fire scenarios, one should focus on model

applicability. For mine fires, the numerical simulation software Fluent2023 can be used to conduct full-scale experiments on tunnel fires. SpaceClaim was employed to create a roadway measuring 200 m in length, 4 m in width, and 3.2 m in height. The meshing process was carried out using Fluent, with a rectangular cut-out measuring 1 m in length and 1 m in width designated as the fire source positioned 100 m from the entrance. The model diagram can be seen in Figure 8.

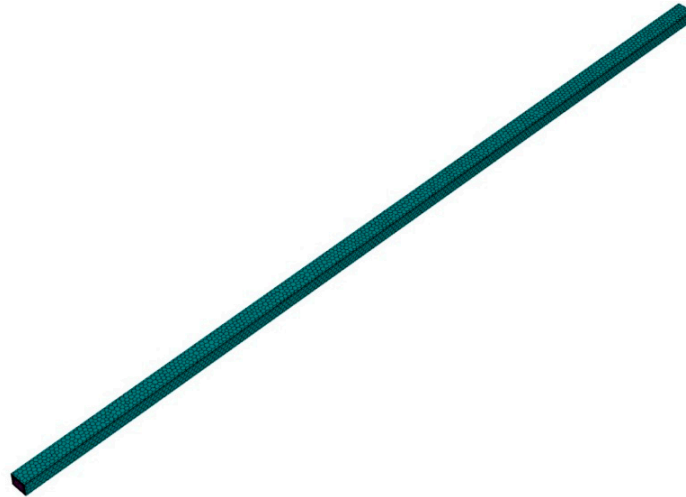
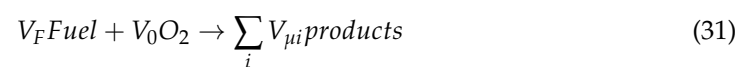
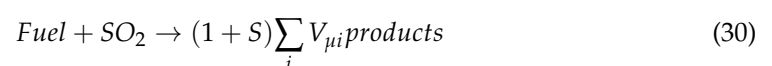


Figure 8. Fluent model diagram.

The simulation setup includes a velocity-inlet for the inlet type, a pressure-outlet for the outlet type, a mass-flow-inlet for the fire source, and a wall for the wall boundary. The turbulence model chosen is the RNG k-epsilon model with consideration for buoyancy, and the P1 radiation model is activated. A monitoring point is positioned directly above the fire source and measurements are taken every 5 m downwind to observe changes in temperature, density, pressure, and wind speed in the specified region.

In order to simplify calculations related to fire source temperature and smoke flow, the combustion reaction equations proposed by Huggett were utilized for the fire source setup. These equations can be described as Equations (30) and (31) [28] (pp. 27–40):



V_i represents the combustible component ratio and S denotes the theoretical oxygen consumption per unit mass of fuel required for complete combustion. Huggett discovered that the rate of heat release during combustion is solely linked to oxygen consumption, with each unit mass of oxygen consumed releasing approximately 1.30 MJ of energy.

Based on the theory mentioned above, when the mass inflow port in Fluent is adjusted to a specific mass flow rate of methane fuel, it results in the consumption of 0.3 kg/m² of methane per second and the release of 1.5 MW/m² of heat. The combustion model in Fluent is configured as a PDF non-premixed combustion model. The fire source location is specified as 0.6 kg/m² of methane fuel per second with a methane mass flow rate of 1. The mixing fraction of methane mass flow into the inlet is set to 1. The oxidant at the ventilation inlet is air, consisting of 0.23 oxygen and 0.77 nitrogen. When the oxidant comes into contact with the fuel, it undergoes rapid combustion, leading to a fast chemical reaction. This model does not account for the specific reaction mechanism, instead focusing on the quick generation of the final combustion product.

5.3. Critical Wind Speed Determination

Critical wind speed is defined as the velocity of wind flow at which the high temperature smoke produced by a fire does not exhibit a backdraft phenomenon. This critical wind speed is typically dependent on factors such as the size of the roadway cross-section, the shape and size of the fire source, among others. In order to further investigate the thermal resistance composition and its changing patterns, numerical simulation experiments are necessary to determine the specific wind speeds involved.

The critical wind speed of a single fire source for this tunnel condition is calculated by the critical wind speed prediction model of WU and Bakar [29] (pp. 364–380), which is as follows:

Baker's prediction model for dimensionless wind speed, calculated by dimensionless treatment of the heat release rate from the fire source, is Equation (32):

$$\begin{cases} v^* = 0.40(0.2)^{-1/3}Q^{*1/3} (Q^* \leq 0.20) \\ v^* = 0.40 (Q^* > 0.20) \end{cases} \quad (32)$$

By calculating the dimensionless wind speed, the critical wind speed can be calculated using the critical wind speed prediction model, which is as in Equation (33):

$$v = v^* \cdot (gH)^{1/2} \quad (33)$$

where v is the critical wind speed, m/s.

Based on the given parameters, it can be inferred that a mass flow rate of approximately 0.6 kg/m^2 per second of methane fuel results in a heat release rate of 3 MW/m^2 . By utilizing Equations (32) and (33), the critical wind speed for this scenario is theoretically around 1.68 m/s . Utilizing Fluent to simulate ventilation speeds of 1.6 m/s , 1.7 m/s , 1.8 m/s , and 1.9 m/s , the critical wind speed was determined to be 1.7 m/s , consistent with the calculated results. Figure 9 illustrates the temperature distribution at both critical and non-critical wind speeds.

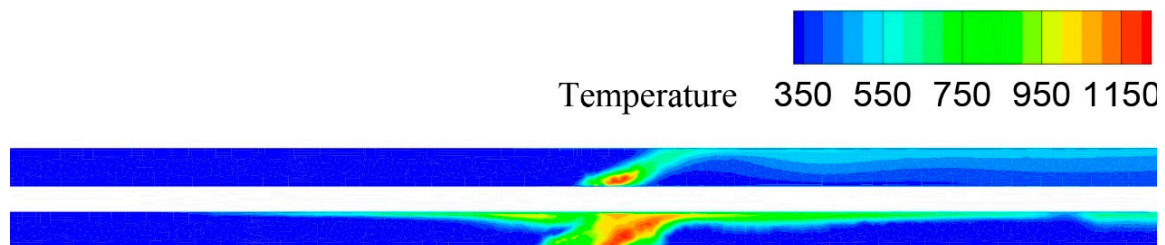


Figure 9. Comparison of 1.6 m/s (bottom) and 1.7 m/s (top) wind speed temperature field.

5.4. Analysis of Numerical Simulation Results

Before commencing the numerical simulation, the full domain is initialized along with the longitudinal wind speed of the tunnel being set at 2 m/s at time 0 s , which exceeds the critical wind speed. Subsequently, the wind speeds at various measurement points within the tunnel are examined, specifically at distances of 10 m , 20 m , 30 m , and 40 m from the fire source. The results are then visualized in a variation diagram depicted in Figure 10.

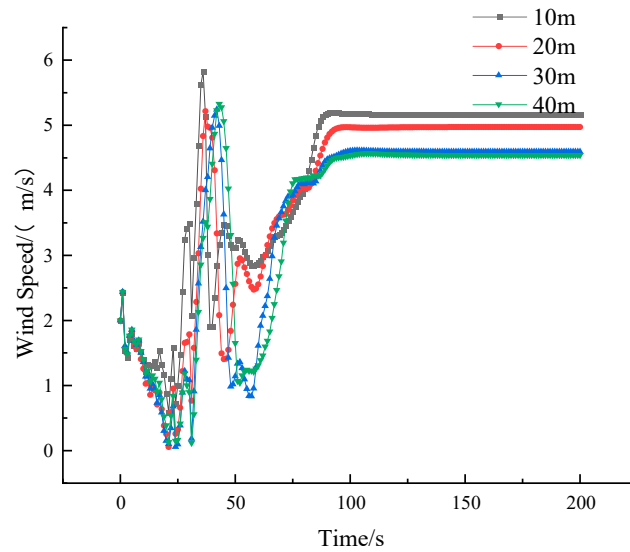


Figure 10. Map of wind speed variations at four monitoring points.

The figure illustrates that during the initial phase of the simulation up to around 90 s, there was fluctuation in wind speed at each measurement point. Beyond 90 s, the wind speed began to stabilize, with a noticeable trend of higher wind speeds closer to the fire source. The wind flow in the heated area increases the internal energy of the fluid and also performs external expansion work due to its physical properties. As the heated wind flow moves through the environment, it transfers heat, overcomes frictional resistance, and experiences a reduction in flow rate and temperature as internal energy decreases. The wind speed is higher at the lower side of the roadway compared to the entrance due to differences in temperature along the roadway causing thermal expansion of the wind flow. The thermal expansion of the fluid is most clearly observed through the decrease in density on the downwind side of the fire source. This phenomenon is illustrated by the density cloud depicted in Figure 11.

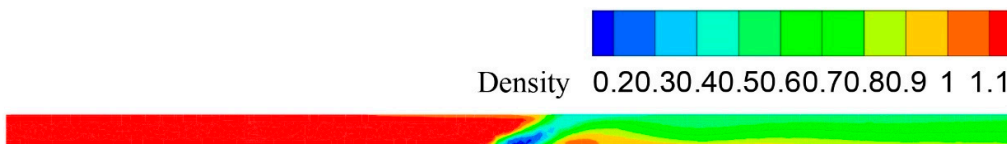


Figure 11. Fire alley density cloud map.

Therefore, the flow velocity on the downwind side of its fire source is always higher than the flow velocity on the upwind side.

Researchers studied the temperature, wind speed, and fire density in the tunnel during the fire stabilization stage to investigate thermal resistance downstream of the fire. Figure 12 depicts the variation in total pressure within the tunnel.

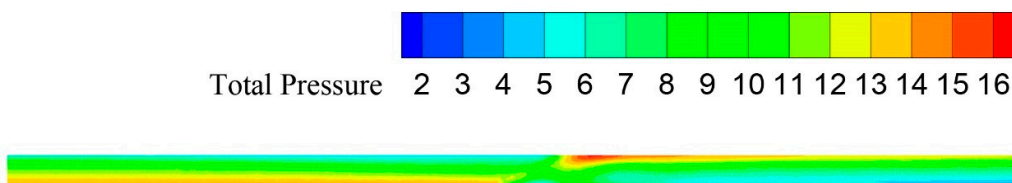


Figure 12. Pressure cloud map of fire tunnel.

In Figure 12, the deflection of the flame front due to wind speed is evident. Pressure stratification is more pronounced on the upwind side of the fire source, as seen in the

same section at the bottom of the roadway where pressure is higher. As vertical height increases, there is a varying degree of pressure reduction. The pressure stratification on the upwind side of the fire source is clearly observable, with higher pressure at the bottom of the roadway and decreasing pressure with height. The flame root creates a wind barrier effect, obstructing the normal wind flow at the bottom of the roadway. This results in the highest pressure at the bottom of the roadway. The continuous area of flame acts like flexible dampers, reducing the movement of wind flow and thereby decreasing ventilation resistance at the bottom. Additionally, as the wind passes through the flame-heated area, the ventilation resistance increases due to thermal resistance, which is temperature-dependent. The high-temperature gas from the fire is influenced by buoyancy force, causing it to accumulate on the downwind side roof of the roadway. Consequently, the roof pressure in the same cross-section is higher than in other areas. The high-temperature smoke flow from the fire diminishes as distance increases, leading to a gradual reduction in thermal resistance and pressure decay, as illustrated in Figure 13.

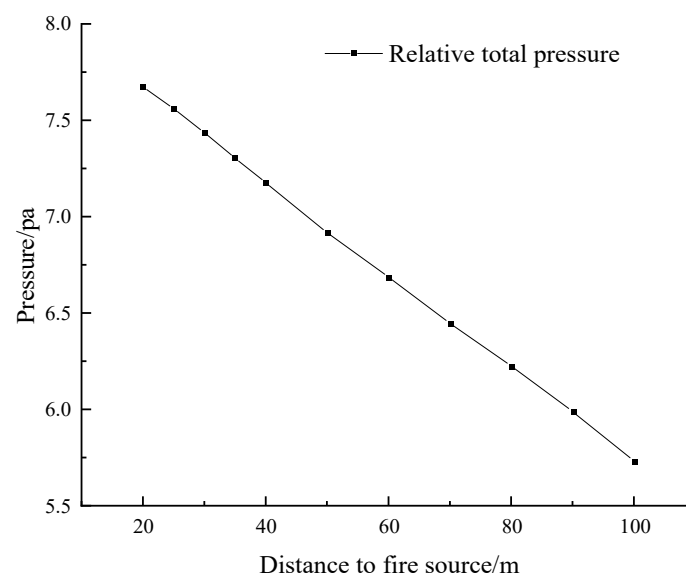


Figure 13. Pressure change chart.

The study illustrated in Figure 13 demonstrates that the thermal resistance caused by the fire decreases as distance increases in a linear fashion. The temperatures, wind speeds, and densities at each monitoring point during the 150 s simulation were collected to validate Equation (28).

The main part of the calculation is the calculation of thermal resistance, which can be expressed by the Formula (34).

$$h_{e,r} = \sum_{i=1}^L \frac{e\rho_{i-1}v_{i-1}^2}{c_p T_{i-1} + e} \cdot \frac{T_i}{T_{i-1}} \quad (34)$$

The interval section is divided into monitoring points based on the modelling data of $L = 100$, $i_{n+1} = i_n + 5$. To assess the accuracy of this equation, the thermal resistance decrease gradients are calculated for each interval. The results are illustrated in Figure 14.

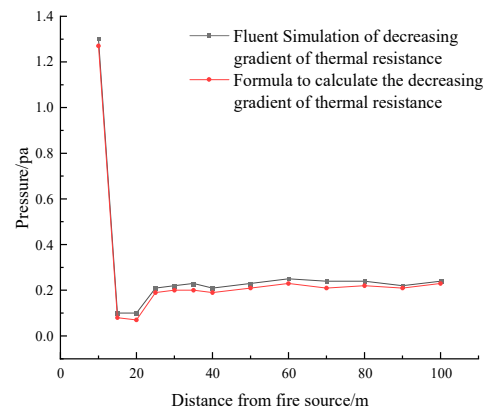


Figure 14. Comparison of simulated and calculated model pressure change gradients.

As illustrated in Figure 14, the numerical simulation results and the thermal resistance trend graph of the constructed mathematical model show a decreasing trend with distance. Upon verification, it was found that the maximum error in the calculated results is within 0.03 pa, representing an error rate of approximately 2.3%. The fit between the results and the numerical simulation is as high as 97.7%, indicating a high level of confidence in the obtained results.

6. Conclusions

1. The components of fire zone resistance are detailed, and the formula for calculating thermal resistance generated by fire is explored through theoretical derivation. Since fire acts as a local heating source, the temperature increase in the roadway due to fire is dependent on the distance. This temperature rise is inversely related to the distance from the fire source. Furthermore, the roadway is divided into intervals to reduce the influence of temperature distribution variations on thermal resistance calculations. This method assists in developing mathematical models for thermal resistance and fire zone resistance in fire tunnels.
2. The temperature change in the tunnel was confirmed through a scaled model experiment and numerical simulation. The peak temperatures of the two methods are 465 °C and 473 °C, respectively, with a difference value of 8 °C. The maximum temperature difference between the two methods was within 20 °C, with a tolerance of no more than 3%. The discrepancy in temperature between the experimental data and numerical simulation can be attributed to calculation errors in the combustion and turbulence models used in the simulation as well as heat loss from the exchange between the scaled model's wall and the environment. This results in the experimental temperature are slightly lower than the simulated temperature, indicating the high credibility of the numerical simulation in replicating fire experiments in the tunnel.
3. Full-scale fire experiments were conducted in the tunnel using Fluent2023 numerical simulation software. Predictive modeling and numerical simulation experiments determined a critical wind speed of 1.7 m/s for this condition. Following the fire event, it was observed that the wind speed downstream of the fire source was higher than at the entrance unaffected by fire due to the fluid properties. Additionally, a negative correlation between wind speed and distance from the fire source was noted, confirming that the change in resistance downstream was temperature-related. It was further established that thermal resistance varies linearly with distance from the fire source.
4. The mathematical model of thermal resistance is validated through numerical simulations, revealing that the resistance gradient between the two calculations decreases by a maximum of 0.03 pa, with an error margin of approximately 2.3%. The model has a high accuracy in calculating thermal resistance, with the fit of its two curves reaching 97.7%. This can serve as the foundation for algorithms used in predicting the location

of fire and providing early warnings by monitoring changes in ventilation resistance in underground mines to enhance fire prevention measures.

Author Contributions: M.N. was in charge of the ideas, formula derivation, and the experimental part of the scaled-down model, and he also conducted the first draft of the paper writing and theoretical validation; X.Z. was responsible for the numerical simulation and theoretical analysis part; W.W. was responsible for the numerical simulation and the experimental accuracy validation part of the downscaled model; Q.Z. was responsible for the data visualization component; H.W. and J.W. were responsible for the collation of articles and correction of errors. All authors have read and agreed to the published version of the manuscript.

Funding: This study was supported by the General Program of the National Natural Science Foundation of China (Grant No. 52064043) and the General Program of the National Natural Science Foundation of China (Grant No. 51764044).

Institutional Review Board Statement: Not applicable.

Informed Consent Statement: Not applicable.

Data Availability Statement: The raw data supporting the conclusions of this article will be made available by the authors on request.

Conflicts of Interest: The authors declare no conflicts of interest.

References

1. Jiang, Y.Q.; Hu, L.H.; Yang, D. Time-Variation Characteristics of Carbon Monoxide Concentration During Transport in Channel Fires. *J. Combust. Sci. Technol.* **2009**, *15*, 273–279.
2. Zhou, C.; Liu, J.; Geng, M.; Wang, D. Study on numerical simulation of thermal resistance in mine ventilation. *J. Saf. Sci. Technol.* **2019**, *15*, 25–31.
3. Zongxiang, L.; Yadi, W.; Guangchao, G. Development of local resistance model of roadway fire flames and parameter identification. *J. China Coal Soc.* **2015**, *40*, 909–914.
4. Ward Smith, A.J. *The Fluid Dynamic of Flow in Pipes and Ducts, Internal Fluid Flow*; Oxford University Press: Oxford, UK, 1980.
5. Peifang, F.; Huaichun, Z.; Qixiang, Y. Study on Parameter Variation Time-sequence in Fire-throttling Process and Its Influence Factors. *J. Saf. Sci. Technol.* **2005**, *7*, 108–112+2.
6. Fu, P.F.; Zhou, H.C.; Yu, Q.X. Study on the fire- throttling process of tunnel fire and its influence factors. *J. China Coal Soc.* **2005**, *2*, 146–150.
7. Fu, P.F.; Zhou, H.C.; Yu, Q.X. Characteristics of Thermal Power and Thermal Resistance During Tunnel Fire Process. *J. China Univ. Min. Technol.* **2004**, *4*, 81–85.
8. Sarvestani, A.N.; Oreste, P. Effects of the Ventilation System by Using Jet Fans during a Fire in Road Tunnels. *Appl. Sci.* **2023**, *13*, 5618. [[CrossRef](#)]
9. Berchtold, F.; Arnold, L.; Knaust, C.; Thöns, S. Uncertainty Modelling in Metamodels for Fire Risk Analysis. *Safety* **2021**, *7*, 50. [[CrossRef](#)]
10. George, D.; Davood, B. *Application of MULTIFLUX for Air, Heat and Moisture Flow Simulations*; Nevada University Press: Reno, NV, USA, 2008.
11. Oka, Y.; Oka, H.; Imazeki, O. Ceiling-jet thickness and vertical distribution along flat ceilinged horizontal tunnel with natural ventilation. *Tunneling Undergr. Space Technol.* **2016**, *53*, 68–77. [[CrossRef](#)]
12. Okayama, Y. A primitive study of a fire detection method controlled by artificial neural net. *Fire Saf. J.* **1991**, *17*, 523–553. [[CrossRef](#)]
13. Okayama, Y. Approach to detection of fires in their very early stage by odor sensors and neural net. *J. Appl. Fire Sci.* **1992**, *2*, 205–217. [[CrossRef](#)]
14. Kalech, B.; Bouterra, M.; ElCafsi, A. Numerical analysis of smoke flow under the effect of longitudinal airflow in a tunnel fire. *Fire Mater.* **2020**, *44*, 1033–1043. [[CrossRef](#)]
15. Wang, H.Y.; Xu, Z.H.; Xu, L.W.; Zhang, B.S. Experimental study on the variation law of wind resistance in branch roadway of fire source during mine fire. *J. Saf. Environ.* **2023**, *23*, 2661–2668.
16. Wala, A.M. Teaching the principles of mine fire using computer aided instruction. *Comput. Appl. Eng. Educ.* **1997**, *5*, 249–255. [[CrossRef](#)]
17. Yang, S.Q. Study on Change Law of Thermal Dynamic of Air Flow and Thermal Resistance in High Temperature and High Humidity Mine. *J. China Coal Soc.* **1997**, *6*, 69–73.
18. Hu, L.H. Studies on Thermal Physics of Smoke Movement in Tunnel Fires. Ph.D. Thesis, University of Science and Technology of China, Hefei, China, 2006.

19. Hu, L.H.; Huo, R.; Wang, H.P.; Li, Y.Z.; Lu, Q.; Yang, L.Z. Judgement on Critical Burning State of Wood Crib from Ventilation-to-Fuel-Controlled Regime by Concentration of Carbon Monoxide in Combustion Products. *J. Combust. Sci. Technol.* **2004**, *4*, 371–374.
20. Hu, L.H.; Huo, R.; Li, Y.Z.; Wang, H.B. Cell-Zone Method: An Engineering Approach to Predict Smoke Movement in Large Scale Building Fire. *Strateg. Study CAE* **2003**, *8*, 59–63.
21. Hu, L.H.; Peng, W.; Yang, R.X. *Fundamentals of Tunnel Fire Dynamics and Prevention Technology*; Science Press: Beijing, China, 2014.
22. Liu, C.; Wan, H.; Ji, J.; Gao, Z.; Lin, S.; Wang, L. Flame Spread Characteristics and a multi-cylinder radiation model for diesel tray fires against a sidewall. *Int. J. Therm. Sci.* **2019**, *139*, 433–439. [[CrossRef](#)]
23. Malalasekera, W.M.G.; Versteeg, H.K.; Gilchrist, K. A review of research and an experimental study on the pulsation of buoyant diffusion flames and pool fires. *Fire Mater.* **1996**, *20*, 261–271. [[CrossRef](#)]
24. Król, A.; Król, M. Some Tips on Numerical Modeling of Airflow and Fires in Road Tunnels. *Energies* **2021**, *14*, 2366. [[CrossRef](#)]
25. Duan, S.Q.; Jiang, X.Q.; Jiang, Q. Theoretical solution and failure analysis of water pressure on lining of deep-buried non-circular hydraulic tunnel based on the equivalent hydraulic radius method. *Eng. Fail. Anal.* **2023**, *148*, 107163. [[CrossRef](#)]
26. Maele, K.V.; Merci, B. Application of RANS and LES field simulations of predict the critical ventilation velocity in longitudinally ventilated horizontal tunnels. *Fire Saf. J.* **2008**, *43*, 598–609. [[CrossRef](#)]
27. Mcgrattan, K.B. Fire modeling where are we? Where are we going? In *Fire Safety Science Proceedings Eighth*, 8th ed.; International Association for Fire Safety Science (IAFSS): Boston, MA, USA, 2005.
28. Shi, W.F. The Numerical Models Research on Mine Fire Smoke Flow and Regularities of Temperature Distribution. Master's Thesis, Taiyuan University of Technology, Taiyuan, China, 2013.
29. Wu, Y.; Baker, M.Z.A. Control of smoke flow in tunnel fires using longitudinal ventilation systems—A study of the critical velocity. *Fire Saf. J.* **2000**, *35*, 363–390. [[CrossRef](#)]

Disclaimer/Publisher's Note: The statements, opinions and data contained in all publications are solely those of the individual author(s) and contributor(s) and not of MDPI and/or the editor(s). MDPI and/or the editor(s) disclaim responsibility for any injury to people or property resulting from any ideas, methods, instructions or products referred to in the content.